Nonlinear Dyn
https://doi.org/10.1007/s11071-025-10889-8

RESEARCH

On estimations of Dawn spacecraft's capture probability into 1:1 ground-track resonance around Vesta

Wail Boumchita · Jinglang Feng · Anatoly Neishtadt

Received: 10 April 2024 / Accepted: 10 January 2025

Abstract This paper develops semi-analytical and analytical methodologies to estimate the probability of the Dawn spacecraft being captured into a 1:1 ground-track resonance around Vesta. The spacecraft, using low-thrust propulsion, approached the asteroid Vesta, and one significant challenge during this phase is crossing ground-track resonances with the asteroid. As the capture phenomenon is dependent on the initial condition of the trajectory, it is necessary to accurately estimate the probability of such a capture. Firstly, the system dynamics are described by a model incorporating Hamiltonian perturbations from the irregular gravitational field up to the second degree and order, and continuous low-thrust that is constant in magnitude and directed in the opposite direction of the spacecraft's velocity. The resonance region is enclosed by separatrices which are approximated with a fourth-order polynomial for quantitative analysis. The Hamiltonian, serving as a proxy for the system's energy, changes when the spacecraft crosses the separatrices, and these changes are quantified using a global adaptive quadrature method. Finally, the probability of capture into ground-track resonance is estimated based on the energy change across the separatrices, and the accuracy and efficiency of the developed semi-analytical and analytical methodologies are investigated by comparing them to numerical simulations based on the perturbed Hamilton's equations of motion. This research makes a significant contribution to the field of astrodynamics by providing a systematic and efficient approach to estimating the probability of resonance capture.

Keywords Semi-analytical methods · Resonance capture · Asteroids · Dawn · Hamiltonian dynamics · Gravitational perturbations · Low-thrust propulsion

Mathematics Subject Classification 70F15 · 70K43 · 37N05

1 Introduction

Resonance, a fundamental concept in dynamical systems, occurs when these systems exhibit amplified oscillations as they are externally perturbed at their inherent natural frequencies. This concept is found across various fields, including but not limited to plasma physics [1], celestial mechanics [2], and astrodynamics [3]. Within celestial mechanics and astrodynamics, different types of orbital resonances exist. These vary from mean-motion resonances, characterized by the orbital periods of two celestial objects hav-

W. Boumchita (✉) · J. Feng
University of Strathclyde, 75 Montrose Street, Glasgow G1 1XJ, UK
e-mail: wail.boumchita@strath.ac.uk

J. Feng
e-mail: jinglang.feng@strath.ac.uk

A. Neishtadt
Loughborough University, Loughborough LE11 3TU, UK
e-mail: a.neishtadt@lboro.ac.uk

Published online: 25 January 2025

ing a simple integer relationship [4], to secular resonances [5], secondary resonances [6], spin-orbit resonances [7], and ground-track resonances (GTRs) [3]. For GTRs to occur, the orbital period of a spacecraft needs to be commensurate with the rotational period of the central celestial body, e.g. geostationary spacecraft orbit Earth in a 1:1 ground-track resonance [8]. Previous studies have delved into the impact of irregular gravitational fields on resonant satellite orbits. Scheeres [9] focused on satellites orbiting irregularly shaped asteroids, particularly investigating periodic orbits around the ellipsoids mimicking asteroids Vesta and Eros. Further studies have extended this research to include asteroid Toutatis [10] and moons such as Europa [11–13] and Enceladus [14,15].

In 2011, the Dawn spacecraft made a successful approach with asteroid Vesta [16]. This mission was among the first to use low-thrust propulsion for both its cruising and approaching stages to an asteroid. It showcased the possibility of using low-thrust systems for extended mission duration [17–19]. While low-thrust propulsion systems, such as those employed by Dawn, offer advantages like fuel efficiency and extended mission duration, they also present unique challenges in designing the spacecraft's trajectory [20]. A primary concern in this context is the potential capture of the spacecraft in a 1:1 GTR [3] with the target asteroid. Delsate [21] found the 1:1 GTR to be the largest GTR that the spacecraft crosses during its descent and for this reason, this paper focuses on this GTR. With each orbital revolution, the spacecraft is exposed to an identical gravitational configuration, the accumulated effects of which substantially modify the spacecraft's orbital parameters like eccentricity and inclination [22,23]. It restricts the spacecraft in descending to lower altitudes, thereby potentially limiting its ability to achieve key scientific observations and data collection.

Given the potential mission-critical implications of GTRs, as illustrated in the Dawn's mission, a detailed investigation into the probability of a spacecraft being captured into such resonances around an asteroid becomes important. The primary aim of this paper is to use the Hamiltonian formalism to analyze the capture into GTR phenomenon and, specifically, estimate the probability of capture in it through semi-analytical and analytical approaches. Our approach is highly adaptable to similar missions: while specific parameters, such as the asteroid's shape and mass or the spacecraft's orbit, may vary across missions, the underlying approach remains consistent. Consequently, our findings and models can be effectively tailored to suit diverse mission scenarios, offering broad applicability in the field of astrodynamics.

The paper is organized as follows: Section 2 provides a description of the unperturbed dynamic model for the motion of Dawn around Vesta and derives the equations of motion and introduces the low-thrust model used in this paper. The semi-analytical and analytical methodologies used to estimate the probability of capture into 1:1 GTR are presented in Sect. 3. The results of these estimations and the comparison with numerical estimations are discussed in Sect. 4, where the errors and computational time are also characterized. This section concludes by showing the advantages of using the analytical methodologies during the mission design phase. Finally, Sect. 5 synthesizes our key findings, offering a concise summary of the study's contributions to the field. This section also identifies avenues for future research, underscoring the ongoing relevance and potential extensions of our work.

2 Dynamical model

In this section, the dynamical environment around Vesta is discussed to identify the key perturbations that influence the spacecraft's motion. Thus, the Hamiltonian that describes the motion of a spacecraft around an asteroid with an irregular gravitational field is formulated. Finally, the impact of non-conservative forces, such as the low-thrust, is derived.

2.1 Main perturbations

In 2011, the Dawn spacecraft reached the asteroid Vesta successfully. As part of its approach phase, the spacecraft descended from a high-altitude mission orbit (HAMO) to a low-altitude mission orbit (LAMO) by using low-thrust propulsion. The orbital distances for HAMO and LAMO are 1000 km and 460 km, respectively [3]. Nevertheless, the use of low-thrust propulsion for the descent stage introduced the risk of the spacecraft being captured in GTRs in the vicinity of Vesta. The asteroid's physical characteristics are presented in Table 1. Vesta is assumed to rotate uniformly about its principal axis of inertia around a constant direction in the inertial frame. The Vesta's unnormal-

ized spherical harmonic coefficients are provided in [24].

The spacecraft is subject to the following perturbations [26]:

– Vesta's irregular gravitational acceleration

$$a_{nm} = (n+1)\frac{\mu}{r^2}\frac{R_e^n}{r^n}J_{nm};$$

where $J_{nm} = \sqrt{C_{nm}^2 + S_{nm}^2}$.

– Sun's gravitational acceleration

$$a_{Sun} = \frac{2\mu_\odot}{d_\odot^3}r;$$

– solar radiation pressure acceleration

$$a_{SRP} = C_r\frac{A}{m}P_\odot$$

where r denotes the spacecraft's distance from Vesta, C_{nm} and S_{nm} are the unnormalized Stokes coefficients, n and m are the degree and order of the spherical harmonic expansion considered, $\mu_\odot$ represents the gravitational constant of the Sun, $d_\odot$ is the distance of the spacecraft from the Sun, $C_r = 0.25$ [3] is the reflectivity coefficient of the spacecraft, $A/m = 0.04$ m^2/kg [3] is the area-to-mass ratio of the spacecraft, and $P_\odot$ is the solar radiation pressure at a distance $d_\odot$ from the Sun. The magnitudes of the main perturbations at different orbital radii are illustrated in Fig. 1.

A detailed analysis of the figure demonstrates that at the orbital radius corresponding to the 1:1 GTR, 537 km, Vesta's second-degree gravitational perturbations are many orders of magnitude stronger than the perturbations from the Sun's gravitational influence and the solar radiation pressure. This highlights the importance of accurately accounting for Vesta's gravitational influence in the dynamical modelling of the spacecraft's trajectory. The zonal harmonics J_{20} and J_{30} are not included as they do not contribute to the phenomenon of 1:1 GTR [8,25]. Furthermore, it is worth noting that the relative magnitudes of these perturbations vary significantly depending on the orbital radius of the spacecraft. Given the dominant effect of Vesta's irregular gravitational perturbations at the 1:1 GTR and the potential impact on the spacecraft's trajectory, in this paper, only these perturbations are considered in the dynamical modelling; solar gravitation and solar radiation pressure are ignored in the following analysis.

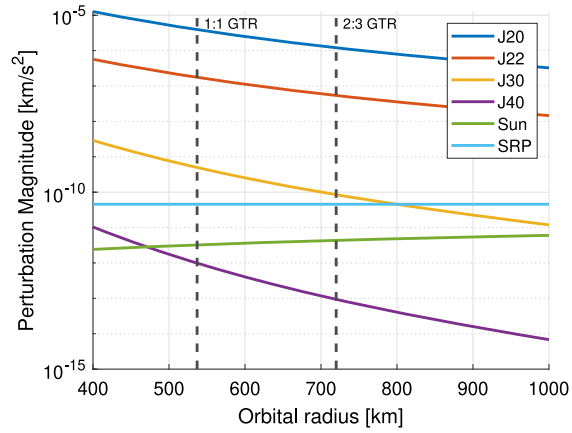

Fig. 1 Order of magnitude of the various perturbations to which the Dawn spacecraft is subject at different orbital radii. The location of the 1:1 and 2:3 GTRs are highlighted for reference

2.2 Hamiltonian model

In celestial mechanics, the spherical harmonics approximation is a commonly used method for characterizing the gravitational field of celestial bodies [26,27]. This method is based on the expansion of the gravitational potential in terms of spherical harmonics, which are a set of orthogonal functions defined on the surface of a sphere. This approach maintains a balance between accuracy and computational cost and has been extensively utilized in prior studies [3,24]. In these studies, the spherical harmonics approximation was employed to model the gravitational fields of various asteroids, including Vesta, 1996 HW1, and Betulia. In this paper, we adopt this methodology to approximate Vesta's irregular gravitational field. The asteroid's shape and density variations are quantitatively captured through the spherical harmonic coefficients [27], which serve as key parameters in defining the gravitational potential. The gravitational potential V is formulated as

$$V = -\frac{\mu}{r} + \sum_{n=2}^{\infty}\sum_{m=0}^{n}\sum_{p=0}^{n}\sum_{q=-\infty}^{\infty} \frac{\mu R_e^n}{a^{n+1}}F_{nmp}(i)G_{npq}(e)S_{nmpq}(\omega, M, \Omega, \theta) \quad (1)$$

where a is the semimajor axis, e is the eccentricity, i is the inclination, $F_{nmp}(i)$ and $G_{npq}(e)$ are functions

Table 1 Vesta's physical parameters [3]

Gravitational constant	μ	17.5 km^3/s^2
Reference radius	R_e	300 km
Angular velocity	$\dot{\theta}$	3.2671×10^{-4} rad/s

dependent on the inclination and eccentricity, respectively. The parameters ω, M, and Ω refer to the argument of periapsis, the mean anomaly, and the longitude of the ascending node respectively, where θ denotes the sidereal angle, n, m, p, q have integer values, and also

$$S_{nmpq} = \begin{cases} C_{nm}\cos\Psi_{nmpq} + S_{nm}\sin\Psi_{nmpq}, & \text{if } n-m \text{ is even} \\ -S_{nm}\cos\Psi_{nmpq} + C_{nm}\sin\Psi_{nmpq}, & \text{if } n-m \text{ is odd} \end{cases}$$

where Ψ_{nmpq} represents Kaula's phase angle defined as

$$\Psi_{nmpq} = (n-2p)\omega + (n-2p+q)M + m(\Omega-\theta) \quad (2)$$

GTRs occur when the rate of change of Kaula's phase angle, $\dot{\Psi}_{nmpq}$, is zero, indicating a commensurability of the spacecraft's orbital period around the asteroid with the asteroid's rotational period around its spin axis. For a spacecraft orbiting an asteroid with an irregular gravitational field, the dynamical behavior of the spacecraft can be described using the Hamiltonian $\mathcal{H}$ formulated as [21]

$$\mathcal{H} = -\frac{\mu^2}{2L^2} + \sum_{n=2}^{\infty}\sum_{m=0}^{n}\sum_{p=0}^{n}\sum_{q=-\infty}^{\infty} R_e^n \frac{\mu^{n+2}}{L^{2n+2}} F_{nmp}(i) G_{npq}(e) S_{nmpq}(\omega, M, \Omega, \theta) + \dot{\theta}\Lambda \quad (3)$$

where $L = \sqrt{\mu a}$ and Λ is the canonically conjugate momentum to θ, and the term $\dot{\theta}\Lambda$ accounts for the asteroid's rotation [21]. The dynamics of the system in the vicinity of the 1:1 GTR are predominantly influenced by the second degree and order gravitational term [28] and, as was done in previous works [25], only this harmonic is considered in the Hamiltonian formulation. The Hamiltonian that captures this dynamic behaviour is

$$\mathcal{H}_{1:1} = -\frac{\mu^2}{2L^2} + R_e^2\frac{\mu^4}{L^6} F_{220}(i) G_{200}(e) S_{2200}(\omega, M, \Omega, \theta) + \dot{\theta}\Lambda \quad (4)$$

According to [27], $F_{220}(i) = \frac{3}{4}(1+\cos i)^2$, $G_{200}(e) = 1 - \frac{5}{2}e^2$ and $S_{2200}(\omega, M, \Omega, \theta) = \cos(2(M+\omega-\theta))$ Thus, in the case of equatorial orbit ($i = 0$), the Hamiltonian takes the form

$$\mathcal{H}_{1:1} = -\frac{\mu^2}{2L^2} - \frac{15}{2}R_e^2\frac{\mu^4}{L^6}\left(-\frac{3}{5} + \frac{G^2}{L^2}\right) C_{22}\cos(2(M+\omega-\theta)) + \dot{\theta}\Lambda \quad (5)$$

where $G = L\sqrt{1-e^2}$. To further simplify the Hamiltonian and analyze the resonant behaviour, a canonical transformation is employed. The generating function used for this transformation, $F = (M+\omega-\theta)L' + (-\omega)G' + \theta\Lambda'$, results in a new set of canonical variables, enabling a more simplified representation of the Hamiltonian and facilitating a more straightforward analysis of the dynamics near the resonance. According to standard formulas for canonical transformation of variables with the generating function F

$$\sigma = \frac{\partial F}{\partial L'} \quad , \quad Q = \frac{\partial F}{\partial G'} \quad , \quad L = \frac{\partial F}{\partial \sigma} \quad , \quad , \quad G = \frac{\partial F}{\partial \omega} \Lambda = \frac{\partial F}{\partial \theta} \quad (6)$$

Thus, the new canonical variable set $(\sigma, L', Q, G', \Lambda)$ is defined as

$$\sigma = M + \omega - \theta \quad , \quad Q = -\omega \quad , \quad L = L' \quad , \quad , \quad G = L' - K \quad \Lambda = -L' + \Lambda' \quad (7)$$

where $K = G' = L - G$. The new Hamiltonian $\tilde{\mathcal{H}}_{1:1}$ is

$$\tilde{\mathcal{H}}_{1:1} = -\frac{\mu^2}{2L^2} - \frac{15}{2}R_e^2\frac{\mu^4}{L^6}\left(-\frac{3}{5} + \frac{(L-K)^2}{L^2}\right) C_{22}\cos(2\sigma) - \dot{\theta}L \quad (8)$$

where $\Lambda' = \text{const}$ and $K = \text{const}$ as the Hamiltonian does not depend on conjugate to them variables, the term $\dot{\theta}\Lambda'$ is omitted and the prime sign is dropped for conciseness. The new Hamiltonian $\tilde{\mathcal{H}}_{1:1}$ provides a clearer understanding of the resonance dynamics. Fig. 2 provides a visual representation of the phase portrait of $\tilde{\mathcal{H}}_{1:1}$. As an example, the case of $e = 0.2$ is considered. To plot the phase-space in Fig. 2, the eccentricity

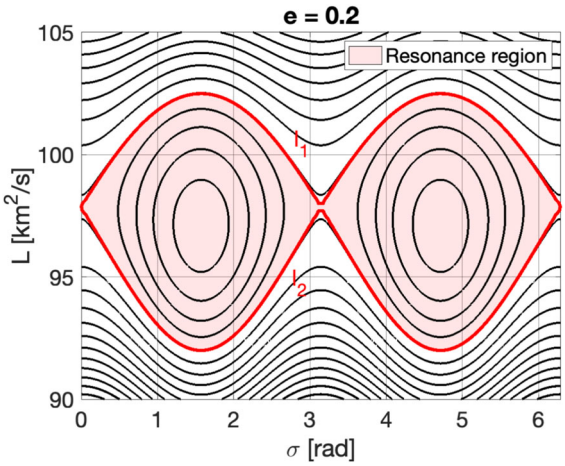

Fig. 2 Phase-space of the 1:1 GTR for $e = 0.2$. The red lines differentiate the separatrix lines, which are indicated as l_1 for the upper separatrix and l_2 for the lower one. The coloured area represents the resonance region

value is determined for a fixed value of K and the value of L at the saddle point as defined in Eq. 11.

The horizontal and vertical axis, labeled as σ and L, cover the range from 0 to 2π and from about 90 to 105 km^2/s, respectively. The contour lines represent energy levels of constant Hamiltonian values in the phase-space. Two bold red lines, labeled l_1 and l_2, are identified. These lines represent the separatrices that define the boundary between the circulation region and resonance region (area highlighted in red) within the phase-space.

2.3 Pendulum approximation

This section introduces a pendulum approximation for the full Hamiltonian model for the 1:1 GTR. This approximation facilitates a more intuitive understanding of the resonance dynamics by reducing the complexity of the Hamiltonian [25,29]. Considering the Hamiltonian from Eq. 8, the Hamiltonian is redefined as

$$\tilde{\mathcal{H}}_{1:1} = -\frac{\mu^2}{2L^2} - A(L, K)\cos(2\sigma) - \dot{\theta}L \tag{9}$$

where

$$A(L, K) = \frac{15}{2}R_e^2\frac{\mu^4}{L^6}\left(-\frac{3}{5} + \frac{(L-K)^2}{L^2}\right)C_{22} \tag{10}$$

The value of L evaluated at the location of the 1:1 GTR, L_r, is determined by

$$\frac{\mu^2}{L_r^3} = \dot{\theta} \tag{11}$$

To analyze the behavior near the resonance, the Hamiltonian is expanded around L_r up to the second order, leading to

$$\hat{\mathcal{H}}_{1:1} = -\frac{1}{2}\alpha p^2 - \hat{A}\cos(2\sigma) \tag{12}$$

where

$$\hat{A} = A(L_r, K) \quad , \quad \alpha = \frac{3\mu^2}{L_r^4} \tag{13}$$

and the constant term is neglected. This expansion simplifies the model while retaining the essential dynamics of the vicinity of the resonance. The resulting Hamiltonian, $\hat{\mathcal{H}}_{1:1}$, resembles the structure of a pendulum's Hamiltonian [30]. It is composed of two principal components: the quadratic term, representing the kinetic energy of a pendulum system, and the cosine term, analogous to the potential energy. This analogy not only simplifies the conceptual understanding of the system's dynamics but also provides further analytical exploration with a familiar framework. Finally, one condition that needs to be satisfied is $\hat{A} \neq 0$, i.e. $e \neq \sqrt{\frac{2}{5}}$. As the eccentricity value approaches $\sqrt{\frac{2}{5}}$, a decrease in the resonance region area is observed until it vanishes at $e = \sqrt{\frac{2}{5}}$. For $e > \sqrt{\frac{2}{5}}$, a growth of the resonance region is noted, accompanied by a shift on the x-axis by $\pi/2$ of the saddle and equilibrium points as illustrated in Fig. 3.

2.4 Dissipative Forces in the Hamiltonian Formalism

Introducing energy dissipation is accomplished by adding dissipative terms to the right hand sides of Hamilton's equations of motion, as discussed in [31]. The time variation of L is expressed in terms of the change in a as

$$\frac{dL}{dt} = \frac{\mu}{2L}\frac{da}{dt} \tag{14}$$

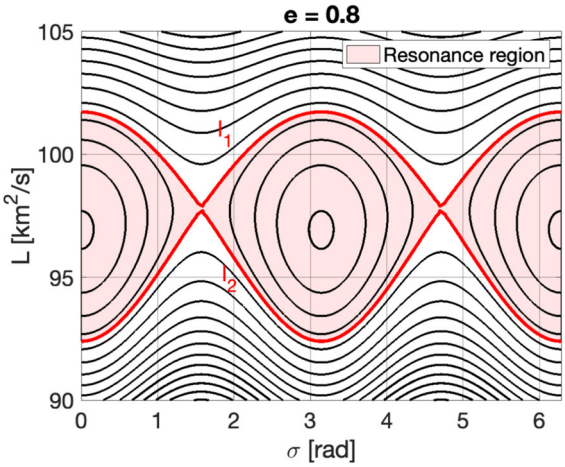

Fig. 3 Phase-space of the 1:1 GTR for $e = 0.8$. The red lines differentiate the separatrix lines, which are indicated as l_1 for the upper separatrix and l_2 for the lower one. The coloured area represents the resonance region

From Eq. 8.2.7 in [32], the averaged over the mean anomaly time derivative of the semi-major axis affected by tangential accelerations is

$$\frac{da}{dt} = 2a_t \frac{a^2}{\mu} < v > \tag{15}$$

where $a_t = -\frac{T}{m}$ represents the magnitude of the tangential acceleration generated by low-thrust maneuvers, v is the spacecraft velocity and $< \cdot >$ denotes averaging over the mean anomaly M. The velocity is obtained from

$$v^2 = \mu \left(\frac{2}{r} - \frac{1}{a} \right) \tag{16}$$

and, with $r = a(1-e\cos E)$ with E being the eccentric anomaly, the expression of the velocity becomes

$$v = \sqrt{\frac{\mu}{a}} \sqrt{\frac{1+e\cos E}{1-e\cos E}} \tag{17}$$

Then, the spacecraft's velocity is averaged over the mean anomaly M as

$$< v >= \frac{1}{2\pi} \int_0^{2\pi} \sqrt{\frac{\mu}{a}} \sqrt{\frac{1+e\cos E}{1-e\cos E}} dM \tag{18}$$

Since $M = E - e\cos E$, the expression of the average of the spacecraft's velocity is

$$< v > = \frac{1}{2\pi} \int_0^{2\pi} \sqrt{\frac{\mu}{a}} \sqrt{\frac{1+e\cos E}{1-e\cos E}} (1-e\cos E) dE = \tag{19}$$

$$= \frac{1}{2\pi} \sqrt{\frac{\mu}{a}} \int_0^{2\pi} \sqrt{1-e^2\cos^2 E} dE = \tag{20}$$

$$= \frac{2}{\pi} \sqrt{\frac{\mu}{a}} \int_0^{\pi/2} \sqrt{1-e^2\cos^2 E} dE = \tag{21}$$

$$= \sqrt{\frac{\mu}{a}} < \hat{v} > \tag{22}$$

where $< \hat{v} >= \frac{2}{\pi} \int_0^{\pi/2} \sqrt{1-e^2\cos^2 E} dE = \frac{2}{\pi}\mathbb{E}(e)$ and $\mathbb{E}(e)$ is the complete elliptic integral of the second kind of e. Therefore, the time variation of L is

$$\frac{dL}{dt} = -\frac{T}{m} \frac{L^3}{\mu^2} \sqrt{\frac{\mu}{a}} < \hat{v} >= \tag{23}$$

$$= -\frac{T}{m} \frac{L^2}{\mu} < \hat{v} > \tag{24}$$

Then, $\frac{dL}{dt}$ is expanded up to the first order with respect to p,

$$\frac{dL}{dt} = -\frac{T}{m} \frac{L_r^2}{\mu} \langle \hat{v} \rangle \big|_{L=L_r} - 2\frac{T}{m} \frac{L_r p}{\mu} \langle \hat{v} \rangle \big|_{L=L_r} - \\ -\frac{T}{m} \frac{L_r^2}{\mu} \frac{\partial}{\partial e^2} < \hat{v} > \left. \frac{\partial e^2}{\partial L} \right|_{L=L_r} p \tag{25}$$

where

$$\frac{\partial e^2}{\partial L} = \frac{\partial}{\partial L} \left[1 - \left(1 - \frac{K}{L} \right)^2 \right] = \tag{26}$$

$$= -2 \left(1 - \frac{K}{L} \right) \frac{K}{L^2} \tag{27}$$

and

$$\frac{\partial}{\partial e^2} < \hat{v} > = -\frac{1}{\pi} \int_0^{\pi/2} \frac{\cos^2 E}{\sqrt{1-e^2\cos^2 E}} dE = \tag{28}$$

$$= -\frac{1}{\pi} \frac{\mathbb{E}(e) - \mathbb{K}(e)}{2e^2} \tag{29}$$

where $\mathbb{K}(e)$ is the complete elliptic integral of the first kind of e. So,

$$\frac{dL}{dt} = -\frac{T}{m} [F_L(K) + D_L(K)p] \tag{30}$$

where

$$F_L = \frac{L_r^2}{\mu}\left\langle \hat{v} \right\rangle\Big|_{L=L_r} \tag{31}$$

$$D_L = \frac{2L_r}{\mu}\left\langle \hat{v} \right\rangle\Big|_{L=L_r} + \frac{L_r^2}{\mu}\frac{\partial}{\partial e^2} < \hat{v} > \left.\frac{\partial e^2}{\partial L}\right|_{L=L_r} \tag{32}$$

For clarity, the variation of L due to the low-thrust is expressed as T_L. Analogously, it is possible to define the time variation of G. The time variation of $G = \sqrt{\mu P}$ is defined as

$$\frac{dG}{dt} = \frac{\mu}{2G}\frac{dP}{dt} \tag{33}$$

where P is the semilatus rectum. From Eq. 8.2.10 in [32], the averaged over the mean anomaly rate of change of P due to tangential low-thrust acceleration is

$$\frac{dP}{dt} = -2\frac{T}{m}P < \frac{1}{v} > \tag{34}$$

From Eq. 22, the average of the inverse of the spacecraft's velocity is derived as

$$< \frac{1}{v} > = \frac{1}{2\pi}\int_0^{2\pi}\sqrt{\frac{a}{\mu}}\sqrt{\frac{1-e\cos E}{1+e\cos E}} (1-e\cos E)dE = \tag{35}$$

$$= \frac{1}{\pi}\sqrt{\frac{a}{\mu}}\int_0^{\pi}\frac{(1-e\cos E)^{3/2}}{\sqrt{1+e\cos E}}dE = \tag{36}$$

$$= \frac{1}{\pi}\sqrt{\frac{a}{\mu}}\int_0^{\pi}\frac{(1-e\cos E)^{2}}{\sqrt{1-e^2\cos^2 E}}dE = \tag{37}$$

$$= \frac{1}{\pi}\sqrt{\frac{a}{\mu}}\int_0^{\pi/2}\left[\frac{(1-e\cos E)^2}{\sqrt{1-e^2\cos^2 E}} + \frac{(1+e\cos E)^2}{\sqrt{1-e^2\cos^2 E}}\right]dE = \tag{38}$$

$$= \frac{2}{\pi}\sqrt{\frac{a}{\mu}}\int_0^{\pi/2}\frac{1+e^2\cos^2 E}{\sqrt{1-e^2\cos^2 E}}dE = \tag{39}$$

$$= \sqrt{\frac{a}{\mu}} < \frac{1}{\hat{v}} > \tag{40}$$

where $< \frac{1}{\hat{v}} > = \frac{2}{\pi}\int_0^{\pi/2}\frac{1+e^2\cos^2 E}{\sqrt{1-e^2\cos^2 E}}dE = \frac{2}{\pi}(2\mathbb{K}(e) - \mathbb{E}(e))$. Therefore,

$$\frac{dG}{dt} = -\frac{T}{m}\frac{LG}{\mu} < \frac{1}{\hat{v}} > \tag{41}$$

Since $G = L - K$ and $L = L_r + p$, it is possible to expand $\frac{dG}{dt}$ up to the first order with respect to p,

$$\frac{dG}{dt} = -\frac{T}{m}\frac{L_r(L_r-K)}{\mu}\left\langle\frac{1}{\hat{v}}\right\rangle\Big|_{L=L_r} - \frac{T}{m}\frac{(2L_r-K)}{\mu}p\left\langle\frac{1}{\hat{v}}\right\rangle\Big|_{L=L_r} - \frac{T}{m}\frac{L_r(L_r-K)}{\mu}\frac{\partial}{\partial e^2} < \frac{1}{\hat{v}} > \left.\frac{\partial e^2}{\partial L}\right|_{L=L_r} p \tag{42}$$

where

$$\frac{\partial}{\partial e^2} < \frac{1}{\hat{v}} > = \frac{2}{\pi}\left(\frac{\mathbb{E}(e)}{e^2(1-e^2)} - \frac{\mathbb{E}(e)+\mathbb{K}(e)}{2e^2}\right) \tag{43}$$

So,

$$\frac{dG}{dt} = -\frac{T}{m}[F_G(K) + D_G(K)p] \tag{44}$$

where

$$F_G = \frac{L_r(L_r-K)}{\mu}\left\langle\frac{1}{\hat{v}}\right\rangle\Big|_{L=L_r} \tag{45}$$

$$D_G = \frac{2L_r-K}{\mu}\left\langle\frac{1}{\hat{v}}\right\rangle\Big|_{L=L_r} + \frac{L_r(L_r-K)}{\mu}\frac{\partial}{\partial e^2} < \frac{1}{\hat{v}} > \left.\frac{\partial e^2}{\partial L}\right|_{L=L_r} \tag{46}$$

As $K = L - G$, the time variation of K due to the low-trust is

$$T_K = T_L - T_G = -\frac{T}{m}[F_K(K) + D_K(K)p] \tag{47}$$

where $F_K = F_L - F_G$ and $D_K = D_L - D_G$. Similarly to the time variation of L, the variation of K due to the low-thrust is expressed as T_K. Finally, the effect of the low-thrust on σ is evaluated as

$$\frac{d\sigma}{dt} = \frac{d}{dt}(M+\omega) \tag{48}$$

Considering that $M = M(E(\nu, e), e)$, where ν is the true anomaly, the expression is expanded as

$$\frac{d\sigma}{dt} = \frac{\partial M}{\partial E}\left(\frac{\partial E}{\partial \nu}\frac{d\nu}{dt} + \left(\frac{\partial E}{\partial e}\right)_{\nu}\frac{de}{dt}\right) + \frac{\partial M}{\partial e}\frac{de}{dt} + \frac{d\omega}{dt} \tag{49}$$

Since $\frac{d\nu}{dt} = -\frac{d\omega}{dt}$ [32], the expression is rearranged as follows

$$\frac{d\sigma}{dt} = \left(-\frac{\partial M}{\partial e}\frac{\partial E}{\partial \nu} + 1\right) T_{\omega} + \left(\frac{\partial M}{\partial E}\left(\frac{\partial E}{\partial e}\right)_{\nu} + \frac{\partial M}{\partial e}\right) T_e \tag{50}$$

where $T_e = \frac{de}{dt}$, $T_{\omega} = \frac{d\omega}{dt}$ and

$$\frac{\partial E}{\partial \nu} = \frac{1 - e\cos E}{\sqrt{1 - e^2}} \quad , \quad \frac{\partial M}{\partial E} = 1 - e\cos E \quad , \quad \frac{\partial M}{\partial e} = -\sin E \tag{51}$$

From Eqs. 8.2.3 and 8.2.4 in [32], the variation of eccentricity and longitude of periapsis over time due to the low-thrust is defined as

$$\frac{de}{dt} = -\frac{2}{v}\frac{T}{m}(e + \cos\nu) \tag{52}$$

$$= -2\sqrt{\frac{a}{\mu}}\frac{T}{m}\sqrt{\frac{1 - e\cos E}{1 + e\cos E}}\frac{(1 - e^2)\cos E}{1 - e\cos E} \tag{53}$$

$$\frac{d\omega}{dt} = -\frac{2}{ev}\frac{T}{m}\sin\nu = \tag{54}$$

$$= -\frac{2}{e}\sqrt{\frac{a}{\mu}}\frac{T}{m}\sqrt{\frac{1 - e\cos E}{1 + e\cos E}}\frac{\sqrt{1 - e^2}\sin E}{1 - e\cos E} \tag{55}$$

From $\tan\frac{\nu}{2} = \sqrt{\frac{1+e}{1-e}}\tan\frac{E}{2}$, it is possible to derive the expression of the rate of change of E with respect to e as follows

$$\frac{\partial}{\partial e}\left(\tan\frac{\nu}{2}\right) = \frac{\partial}{\partial e}\left(\sqrt{\frac{1+e}{1-e}}\right)\tan\frac{E}{2} + \sqrt{\frac{1+e}{1-e}}\frac{\partial}{\partial e}\left(\tan\frac{E}{2}\right) \tag{56}$$

So,

$$\left(\frac{\partial E}{\partial e}\right)_{\nu} = -2\sqrt{\frac{1 - e}{1 + e}}\cos^2\frac{E}{2}\frac{\partial}{\partial e}\left(\sqrt{\frac{1 + e}{1 - e}}\right)\tan\frac{E}{2} \tag{57}$$

Given that

- $\frac{\partial E}{\partial \nu}$ is an even function of E;
- $\frac{\partial M}{\partial E}$ is an even function of E;
- $\frac{\partial e}{\partial t}$ is an even function of E;
- $\frac{\partial M}{\partial e}$ is an odd function of E;
- $\frac{\partial E}{\partial e}$ is an odd function of E;
- $\frac{\partial \omega}{\partial t}$ is an odd function of E;

it can be concluded that $\frac{d\sigma}{dt}$ is an odd function of E and its average over M is zero. Thus, the low-thrust does not affect the evolution of σ. Introducing the variable $p = L - Lr$, the perturbed Hamilton's equations of motion become

$$\begin{cases} \dot{\sigma} = \frac{\partial \tilde{\mathcal{H}}_{1:1}}{\partial p} \\ \dot{p} = -\frac{\partial \tilde{\mathcal{H}}_{1:1}}{\partial \sigma} + T_L \\ \dot{K} = T_K \end{cases} \tag{58}$$

where the first equation does not have any perturbation term, since it is proven that the low-thrust does not affect the evolution of σ. For the numerical propagation of the trajectories the complete Hamiltonian model $\tilde{\mathcal{H}}_{1:1}$ is used. While σ and p have a clear physical meaning, K does not have a clear physical meaning. It is an intermediate quantity to facilitate mathematic derivations. It is a quantity which is dependent on both the semimajor axis and eccentricity represented by the variables L and G, respectively. It is possible to consider it as a conservation law for the system. In fact, $K = const$ for $T = 0$. Figure 4 shows a numerical validation of the resonance capture phenomenon for $e_0 = 0.2$. Initial resonance angles are uniformly distributed in the range [0,2π], and a semi-major axis value of 700 km is adopted as the initial condition.

The numerical simulation results suggest a resonance capture of the spacecraft, as highlighted in red in Fig. 4. This capture is represented in the top-left plot of Fig. 4, where the momentum L undergoes libration about the resonance point at $L = L_r$. The top-right plot of Fig. 4 offers a phase portrait that showcases the system's trajectory in phase-space. Herein, the trajectory in resonance revolves around the stable equilibrium point (σ,L) = (π/2,L_r). As the system evolves, the Delaunay action K increases, as illustrated in the bottom-left plot. Similarly, the eccentricity e increases over time as shown in the bottom-right plot. The growth of the eccentricity e can be explained as follows. The rate of change of e is the sum of two terms: the Hamil-

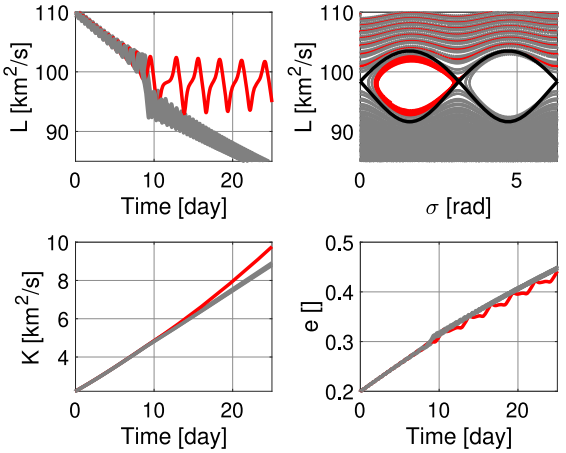

Fig. 4 Evolution of trajectory over time for the case of 1:1 GTR crossing. Capture cases and the separatrices are highlighted in red and in black, respectively. The top diagrams show the evolution of $L = p + L_r$ over time and in phase-space. The lower diagrams show the variations of K and eccentricity with time, respectively

tonian one (due to the gravitational potential of the asteroid) and non-Hamiltonian (due to the thrust). The former term produces only oscillations of the eccentricity. while the latter causes the secular evolution of the eccentricity. Its rate is given by Eq. 53 via averaging over the mean anomaly M

$$\frac{de}{dt} = -\frac{1}{\pi}\sqrt{\frac{a}{\mu}}\frac{T}{m}\int_0^{2\pi}\sqrt{\frac{1-e\cos E}{1+e\cos E}}\frac{(1-e^2)\cos E}{1-e\cos E}dM \tag{59}$$

$$= -\frac{1}{\pi}\sqrt{\frac{a}{\mu}}\frac{T}{m}\int_0^{2\pi}\sqrt{\frac{1-e\cos E}{1+e\cos E}}\frac{(1-e^2)\cos E}{1-e\cos E}(1-e\cos E)dE \tag{60}$$

$$= -\frac{2}{\pi}\sqrt{\frac{a}{\mu}}\frac{T}{m}(1-e^2)\int_0^{\pi}\sqrt{\frac{1-e\cos E}{1+e\cos E}}\cos E dE \tag{61}$$

$$= -\frac{2}{\pi}\sqrt{\frac{a}{\mu}}\frac{T}{m}(1-e^2)\int_0^{\pi/2}\left(\sqrt{\frac{1-e\cos E}{1+e\cos E}} - \sqrt{\frac{1+e\cos E}{1-e\cos E}}\right)\cos E dE \tag{62}$$

$$= \frac{1}{\pi}\sqrt{\frac{a}{\mu}}\frac{T}{m}(1-e^2)\int_0^{\pi/2}\frac{4e\cos^2 E}{\sqrt{1-e^2\cos^2 E}}\cos E dE \tag{63}$$

Therefore, as T is the thrust magnitude and it is always positive, the eccentricity increases in average over time for $e \neq 0$. Finally, it is observed that the growth of the eccentricity leads to an important phenomenon in the behaviour of the periapsis. The radius of periapsis is $r_p = a(1-e)$. The semi-major axis a either decays on average (when the spacecraft is not captured into the resonance) or oscillates about $a_r = L_r^2/\mu$ (when the spacecraft is captured in the resonance). Thus, the growth of the eccentricity leads to a secular decay of r_p, which in turn may lead to the collision of the spacecraft with the asteroid. This should be considered in planning missions similar to that of Dawn.

3 Methodology

This section explores into the semi-analytical methodology employed to estimate the probability of capture into a 1:1 GTR. The phase-space region, denoted by U and defined by the canonical coordinates (σ, p), is defined such that the initial conditions are uniformly distributed within it. In this region, a specific subset of initial conditions, denoted as U_{res}, is distinguished. These conditions result in the system's confinement within the resonance region. The probability of capture into this resonance is expressed as [33]

$$Pr = \frac{\text{mes}U_{res}}{\text{mes}U} \tag{64}$$

where $\text{mes}U_{res}$ and $\text{mes}U$ represent the volumes of the regions U_{res} and U in phase-space, respectively. It is important to note that the above formulation is specifically defined for a numerical evaluation of the probability. From an analytical standpoint, the probability needs to be adapted using energy-related attributes of the system. Drawing upon insights from [34], the probability of capture into 1:1 GTR is formulated as

$$Pr = \frac{\int_{l_1\cup l_2}\frac{d\tilde{\mathcal{H}}_{1:1}}{dt}dt}{\int_{l_1}\frac{d\tilde{\mathcal{H}}_{1:1}}{dt}dt} \tag{65}$$

where $\int_{l_1\cup l_2}$ represents an line integration along both l_1 and l_2 and $\int_{l_1}$ indicates the line integral along l_1 exclusively. Indicating $\tilde{\mathcal{H}}_{SP}$ as the Hamiltonian $\tilde{\mathcal{H}}_{1:1}$ from Eq. 8 evaluated at the separatrix's saddle point,

the Hamiltonian is normalized as

$$\tilde{\tilde{\mathcal{H}}}_{1:1} = \tilde{\mathcal{H}}_{1:1} - \tilde{\mathcal{H}}_{SP} \tag{66}$$

This normalization is required because the trajectory evolution in phase-space along the separatrix is characterized and can last for an infinite time duration as explained in [33,34]. Hence, by normalizing the Hamiltonian, convergence of the integrals is guaranteed. As is mentioned in Sect. 2.3, the phase portrait is different depending on the value of the eccentricity. Thus in the following sections, the case of $e < \sqrt{\frac{2}{5}}$ is considered.

3.1 Full model

The methodology used to estimate the probability relies upon the normalized full Hamiltonian model from Eq. 66. Firstly, the values of p associated with the separatrices, denoted as p_{sep}, are approximated numerically using an N-th order polynomial function

$$p_{sep} = \sum_{i=0}^{N} c_i(K)\sigma^i \tag{67}$$

where $c_i(K)$ are the coefficients of the polynomial, and σ is the variable of the function. Here, the coefficient K is fixed at K_{sep}, the value corresponding to the trajectory's intersection with the separatrix. The determination of K_{sep} involves numerically solving the perturbed Hamilton's equations for various initial conditions to identify the separatrix crossings. This process consists in comparing the Hamiltonian's value at each instant with its value at the separatrix to ascertain K_{sep} for the i-th trajectory. The average of these K^i_{sep} values is then calculated to establish K_{sep}. An investigation into the appropriate order of the polynomial for approximating the separatrices reveals that a 4th-order polynomial suitably approximates the separatrices, as shown in Fig. 5, where the black dashed lines effectively approximate the separatrix (in red).

Since the upper and lower separatrices have different shapes, these functions are further classified into lower and upper separatrices, labelled as p^{low}_{sep} and p^{up}_{sep}, respectively. Considering Eq. 65, the denominator's

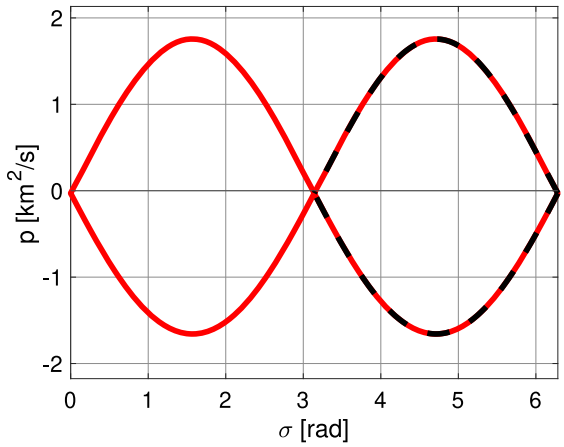

Fig. 5 Separatrices (in red) and their approximation p_{sep} (in black)

integral argument is developed as

$$\frac{d\tilde{\tilde{\mathcal{H}}}_{1:1}}{dt} = \frac{\partial\tilde{\tilde{\mathcal{H}}}_{1:1}}{\partial\sigma}\frac{\partial\sigma}{\partial t} + \frac{\partial\tilde{\tilde{\mathcal{H}}}_{1:1}}{\partial p}\frac{\partial p}{\partial t} + \frac{\partial\tilde{\tilde{\mathcal{H}}}_{1:1}}{\partial K}\frac{\partial K}{\partial t} \tag{68}$$

Substituting the perturbed Hamilton's equation of motion from Eq. 58, the Hamiltonian time derivative is

$$\begin{aligned}\frac{d\tilde{\tilde{\mathcal{H}}}_{1:1}}{dt} &= \frac{\partial\tilde{\tilde{\mathcal{H}}}_{1:1}}{\partial\sigma}\frac{\partial\tilde{\tilde{\mathcal{H}}}_{1:1}}{\partial p} - \frac{\partial\tilde{\tilde{\mathcal{H}}}_{1:1}}{\partial p}\frac{\partial\tilde{\tilde{\mathcal{H}}}_{1:1}}{\partial\sigma} \\ &\quad + \frac{\partial\tilde{\tilde{\mathcal{H}}}_{1:1}}{\partial p}T_L + \frac{\partial\tilde{\tilde{\mathcal{H}}}_{1:1}}{dK}T_K \qquad (69)\\ &= \frac{\partial\tilde{\tilde{\mathcal{H}}}_{1:1}}{\partial p}T_L + \frac{\partial\tilde{\tilde{\mathcal{H}}}_{1:1}}{\partial K}T_K \qquad (70)\end{aligned}$$

Thus,

$$\int_{l_1}\frac{d\tilde{\tilde{\mathcal{H}}}_{1:1}}{dt}dt = \int_{l_1}\frac{\partial\tilde{\tilde{\mathcal{H}}}_{1:1}}{\partial p}T_L dt + \int_{l_1}\frac{\partial\tilde{\tilde{\mathcal{H}}}_{1:1}}{\partial K}T_K dt = \tag{71}$$

$$= \int_{l_1}\frac{\partial\tilde{\tilde{\mathcal{H}}}_{1:1}}{\partial p}T_L\frac{1}{\frac{d\sigma}{dt}}d\sigma + \int_{l_1}\frac{\partial\tilde{\tilde{\mathcal{H}}}_{1:1}}{\partial K}T_K\frac{1}{\frac{d\sigma}{dt}}d\sigma \tag{72}$$

Substituting the expression of $d\sigma/dt$ from the perturbed Hamilton's equations of motion Eq. 58, the inte-

gral is expressed as

$$\int_{l_1} \frac{d\,\tilde{\tilde{\mathcal{H}}}_{1:1}}{dt} dt = \int_{\pi}^{0} T_L d\sigma + \int_{\pi}^{0} \frac{\partial\,\tilde{\tilde{\mathcal{H}}}_{1:1}}{\partial K} \frac{1}{\frac{\partial\,\tilde{\tilde{\mathcal{H}}}_{1:1}}{\partial p}} T_K d\sigma \tag{73}$$

This expression is then evaluated at $p = p_{sep}^{up}(\sigma)$ since the expression is integrated along the upper separatrix, and numerically integrated employing the global adaptive quadrature technique as outlined in [35]. This technique divides the integration domain into subintervals, approximating the integral as the sum of their contributions. The subinterval sizes are dynamically adjusted to minimize approximation errors. The numerator of the equation is derived as

$$\int_{l_1 \cup l_2} \frac{d\,\tilde{\tilde{\mathcal{H}}}_{1:1}}{dt} dt = \int_{l_1} \frac{d\,\tilde{\tilde{\mathcal{H}}}_{1:1}}{dt} dt + \int_{l_2} \frac{d\,\tilde{\tilde{\mathcal{H}}}_{1:1}}{dt} dt \tag{74}$$

The first term is the same as in the denominator. The second one is developed similarly as

$$\int_{l_2} \frac{d\,\tilde{\tilde{\mathcal{H}}}_{1:1}}{dt} dt = \int_{0}^{\pi} T_L d\sigma + \int_{0}^{\pi} \frac{\partial\,\tilde{\tilde{\mathcal{H}}}_{1:1}}{\partial K} \frac{1}{\frac{\partial\,\tilde{\tilde{\mathcal{H}}}_{1:1}}{\partial p}} T_K d\sigma \tag{75}$$

evaluated at the curve $p = p_{sep}^{low}(\sigma)$, since the expression is integrated along the lower separatrix. It is important to notice that the integration along l_1 is performed from π to 0 while the integration along l_2 is performed from 0 to π, as this is the direction in which the trajectory evolves in phase-space. Referencing to the upper right plot of Fig. 4, the trajectory in phase-space evolves from right to left. As the trajectory approaches the resonance region, it evolves along the upper separatrix l_1 from 2π to π, while along the lower separatrix l_2 from π to 2π. Since the period of the Hamiltonian is π, the integral is done in the interval from 0 to π.

3.2 Pendulum approximation

Similar to the full model, the Hamiltonian value undergoes normalization, yielding $\hat{\tilde{\mathcal{H}}}_{1:1} = \hat{\mathcal{H}}_{1:1} - \hat{A}$, where $\hat{A}$ is defined in Eq. 13. Consequently, the new Hamiltonian, $\hat{\tilde{\mathcal{H}}}_{1:1}$, is represented as

$$\hat{\tilde{\mathcal{H}}}_{1:1} = -\frac{1}{2}\alpha p^2 + 2\hat{A}\sin^2\sigma \tag{76}$$

The rate of change of $\hat{\tilde{\mathcal{H}}}_{1:1}$ is determined as

$$\frac{d\hat{\tilde{\mathcal{H}}}_{1:1}}{dt} = -\alpha p\, T_L + 2\frac{d\hat{A}}{dK}\sin^2\sigma\, T_K \tag{77}$$

So, the probability of capture is

$$Pr = \frac{\int_{l_1\cup l_2} -\alpha p\,[F_L(K) + D_L(K)p] + 2\frac{d\hat{A}}{dK}\sin^2\sigma\,[F_K(K) + D_K(K)p]\,dt}{\int_{l_1} -\alpha p\,[F_L(K) + D_L(K)p] + 2\frac{d\hat{A}}{dK}\sin^2\sigma\,[F_K(K) + D_K(K)p]\,dt} \tag{78}$$

The expression needs to be evaluated along the separatrix. It is noted that the equation remains unaffected by both the spacecraft mass and the thrust magnitude since both T and m are cancelled from the equation as they were included in each term of the equation. Imposing the condition $\hat{\tilde{\mathcal{H}}}_{1:1} = 0$, it follows that

$$p_{sep} = \pm 2\sqrt{\frac{\hat{A}}{\alpha}}\sin\sigma \tag{79}$$

The pendulum model has the same shape of upper and lower separatrices. Thus, there is no need to distinguish between p_{sep}^{low} and p_{sep}^{up} as for the full model. Upon combining Eq. 77 and Eq. 79, the probability of achieving a 1:1 GTR capture is

$$Pr = \frac{8\sqrt{\frac{\hat{A}}{\alpha}}D_L - 4\frac{\partial\hat{A}}{\partial K}\frac{1}{\sqrt{\hat{A}\alpha}}F_K}{\pi F_L + 4\sqrt{\frac{\hat{A}}{\alpha}}D_L - 2\frac{\partial\hat{A}}{\partial K}\frac{1}{\sqrt{\hat{A}\alpha}}F_K - \frac{\pi}{\alpha}\frac{\partial\hat{A}}{\partial K}D_K} \tag{80}$$

The advantage of using the pendulum model is the fact that it is possible to formulate analytically the expression of the probability of capture, which is not possible to do for the full model.

4 Results

In this section, three different methodologies - numerical, semi-analytical, and analytical - are presented and compared. The probability of capture is estimated across two thrust magnitude ranges: high thrust magnitude cases with $T = [0.2, 20]$ mN, and small thrust magnitude cases with $T = [0.02, 0.2]$ mN. If not otherwise stated, the initial conditions for the simulations are listed in Table 2. In particular, for the semimajor axis, a small interval is chosen far enough considering the location of the resonance.

4.1 Simulation setup

For numerical estimation of the probability of capture, 1000 different trajectories are propagated using the perturbed Hamilton's equations of motion from Eq. 58 where the initial conditions are included inside the interval of initial conditions defined in Table 2. The initial conditions are sampled across the intervals: 100 different initial semi-major axis values and 10 different resonance angle values. The chosen semi-major axis range can be changed with the only condition that it has to be far enough from the resonance region. The equations of motion are propagated for 20 days using the MATLAB built-in function `ode113` which is a variable-step, variable-order Adams-Bashforth-Moulton solver of orders 1 to 13 [36], with a relative and absolute tolerance of 10^{-12}. The mean probability of capture is obtained by averaging the probability obtained for 100 different thrust magnitude values for 1000 trajectories with different initial conditions. The simulations are performed in MATLAB's Parallel Computing Toolbox on a Macbook M3 Pro with an 11-core CPU (5 performance cores and 6 efficiency cores).

4.2 Sensitivity on the thrust magnitude

The probability estimations obtained using the three approaches are compared and presented in Fig. 6.

In the two plots, the probability of capture into 1:1 GTR for $e = 0.1$ is distinguished by colour: the black line represents the probability estimated numerically, the red line represents the semi-analytical estimation, obtained with Eq. 65 considering the Hamiltonian from Eq. 66, and the blue line represents the analytical estimation, obtained with Eq. 80 considering the Hamiltonian from Eq. 76. Over the entire range of thrust magnitudes, a lack of dependence of the probability on thrust magnitude is demonstrated by the analytical estimation, which maintains a value of around 10.33%. Similarly, the semi-analytical estimation also exhibits independence from thrust magnitude and has a similar value of 10.13%. The probability of capture is accurately estimated by both methodologies and in Section 4.3 this analysis is expanded to different values of eccentricity. With increasing thrust magnitudes, a noticeable decrease in the mean probability of capture is noted, as shown by the numerical estimations. This trend is not reflected in the estimations provided by the semi-analytical and analytical methods. This is briefly described after Eq. 80, where each term of the analytical formulation of the probability of capture is free from any term related to the low-thrust. For this reason, in the last part of the paper, the thrust magnitude interval between 0.02 and 0.2 mN is considered.

4.3 Sensitivity on the eccentricity

This section is dedicated to examining how variations in initial eccentricity impact the probability of spacecraft capture into a 1:1 GTR. Under the setup presented in Section 4, the probability of capture into a 1:1 GTR is estimated across a range of eccentricity values from 0.025 to 0.5 to include a broad spectrum of possible orbital scenarios. Table 3 summarizes the probability values obtained with the three methodologies.

Figure 7 illustrates the mean probability of capture for eccentricities ranging from 0.025 to 0.5.

The numerical probability estimation for $e = 0.025$ is about 12.10%. It is observed that both semi-analytical and analytical methodologies estimate accurately the probability of capture for the entire range of eccentricities considered. A general trend is identified: as the eccentricity value increases, the probability of capture decreases.

For $e_0 > 0.4$, the probability of capture drops to zero. Additionally, for captured cases at $e < \sqrt{\frac{2}{5}}$, the eccentricity grows, A decays, and thus the spacecraft should leave the regime of capture eventually as shown in Fig. 8.

Table 2 Range of initial conditions for the numerical simulations

Resonance angle	$[0, 2\pi]$
Semimajor axis	[690,700] km
Eccentricity	[0.025, 0.5]

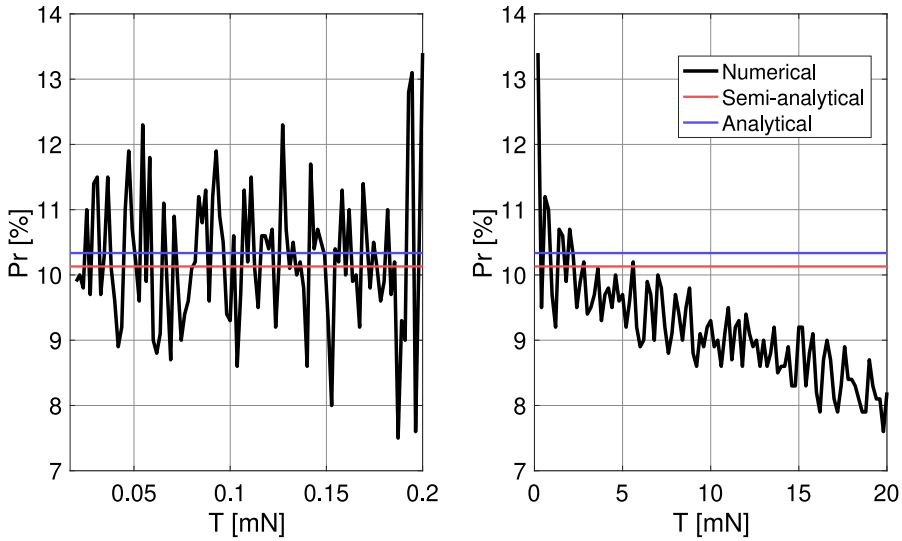

Fig. 6 Probability of capture into 1:1 GTR evolution for $e = 0.1$ and for different thrust magnitude values estimated with numerical (in black), semi-analytical (in red) and analytical (in blue) methodologies. small thrust and high thrust cases are shown in the left and right plots, respectively

Table 3 Probability estimations comparison between numerical, semi-analytical, and analytical methodologies for different eccentricity values

Eccentricity [-]	Numerical [%]	Semi-analytical [%]	Analytical [%]
0.025	12.10	12.22	12.53
0.05	11.49	11.27	11.56
0.1	10.25	10.13	10.33
0.2	6.96	6.55	6.60
0.3	0.25	0.10	0.47
0.4	0	0	0
0.5	0	0	0

These results arise because the numerator in both the semi-analytical and analytical formulations of the probability becomes negative.

4.4 Computational time

This subsection compares the computational times required by numerical, semi-analytical, and analytical approaches in estimating the probability of capture into a 1:1 GTR. Computational efficiency is one of the driving factors in selecting a suitable methodological approach. The numerical approach calculates the cap-

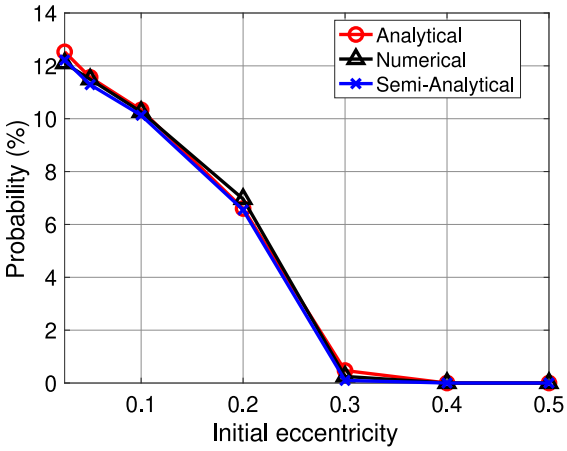

Fig. 7 Mean probability of capture into 1:1 GTR evolution for low thrust magnitude values and for different eccentricity values estimated with numerical (in black), semi-analytical (in blue) and analytical (in red) methodologies

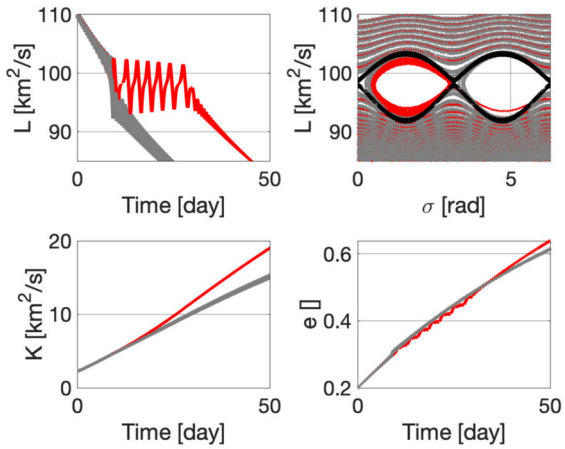

Fig. 8 Evolution of trajectory over 50 days for the case of 1:1 GTR crossing. Capture cases and the separatrices are highlighted in red and in black, respectively. The top diagrams show the evolution of $L = p + L_r$ over time and in phase-space. The lower diagrams show the variations of K and eccentricity with time, respectively

ture probability by propagating Hamilton's equations of motion and determining the ratio of initial conditions leading to capture over the total number of initial conditions. In contrast, the analytical approach requires significantly fewer computational resources, with the semi-analytical method positioned between the two in terms of resource demand. Table 4 presents a comparison of computational times across different eccentricity levels for each method.

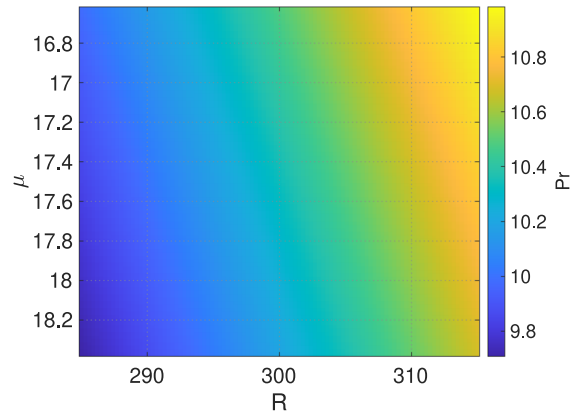

Fig. 9 Probability of capture into 1:1 GTR for a range of μ and R with $e = 0.1$

The computational time of the numerical approach is significantly higher than that of the semi-analytical and analytical one, clearly indicating the advantage of the methodologies developed in this research. Given its comparable accuracy and reduced computational demand, the analytical method is recommended for preliminary mission analysis and design.

4.5 Uncertainty analysis

The analytical methodology allows for an efficient analysis of the probability of capture in the case in which the physical property values of the asteroid are affected by uncertainty. An example is shown in this section. Assuming a 5% uncertainty on both μ and R, it is possible to analyze the change of probability of capture for a specific eccentricity value. Figure 9 shows the result of such analysis.

The color gradient represents the magnitude of the probability, with the color bar indicating the scale. Yellow or lighter shades correspond to higher probabilities, while darker shades indicate lower probabilities. An increase in the probability of capture is observed with the increase of R, whereas an increase in μ leads to a decrease in the probability of capture. Specifically, a 5% uncertainty in both parameters yields a probability range of approximately [9.71, 10.98]% and the computational time required for such analysis is around 0.35 seconds. However, the behavior of the probability varies depending on the considered eccentricity value. This is shown in Fig. 10, where the analysis is conducted for $e_0 = 0.3$.

Table 4 Computational time comparison among numerical, semi-analytical, and analytical methods for different eccentricity values

Eccentricity	Numerical [s]	Semi-analytical [s]	Analytical [s]
0.025	101467	2.08	0.0058
0.05	99033	1.58	0.0002
0.1	94780	1.74	0.0003
0.2	83218	1.74	0.0002
0.3	70729	1.70	0.0004
0.4	48609	1.61	0.0002
0.5	35115	1.61	0.0002

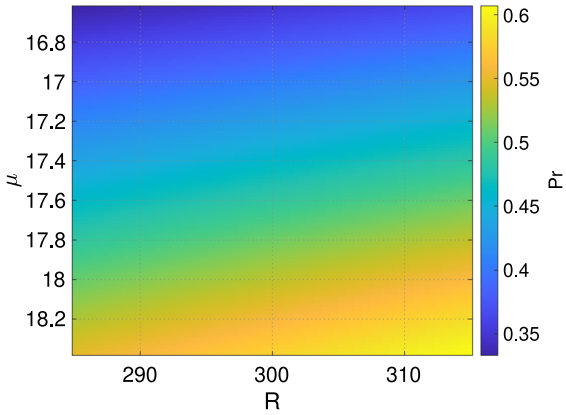

Fig. 10 Probability of capture into 1:1 GTR for a range of μ and R with $e = 0.3$

In this instance, the probability of capture is observed to increase with μ. So, a general trend cannot be established, necessitating the analysis of each case independently. This issue emphasizes the need for a more efficient method to estimate the probability of capture. The same analysis can be extended to all four physical parameters characterizing the asteroid (μ, R, C_{22}, ω), as shown in Fig. 11, where it is assumed a 5% uncertainty on each parameter.

Each of the plots varies two parameters while keeping the others fixed, showing how the probability of capture changes with these parameters. Finally, Fig. 12 summarizes each one of these plot in a single plot showing the mean, minimum and maximum range of probabilities considering an uncertainty of 5% on every parameter.

It is noticed that the higher the probability the higher the uncertainty of such probability. In particular, at lower eccentricities, the model exhibits an uncertainty of approximately 2.93%, which is the highest. This value decreases progressively as the eccentricity increases. When the eccentricity is increased further, the absolute uncertainty drops to zero at the higher eccentricity values. This methodology allows mission analysts to conduct comprehensive analyses on the GTR capture phenomenon, thereby enhancing the robustness of exploration missions against this phenomenon.

5 Conclusion

This study develops three methodologies, i.e. the numerical, semi-analytical, and analytical ones, to estimate the probability of capture into the 1:1 GTR for low-thrust spacecraft moving around an asteroid. A perturbed Hamiltonian model is developed, considering the asteroid's irregular gravitational field represented by a spherical harmonic approximation, and the effect of low-thrust propulsion. The general formulation of the probability of capture is presented and applied to this model for numerical estimations. The formulation is further developed for semi-analytical estimations relying on energy-based quantities like the Hamiltonian. Finally, an approximation of the Hamiltonian model is developed by expanding it around the location of the resonance, which is used to develop the analytical formulation for the probability of capture. The analysis indicates that for small thrust values, the semi-analytical and analytical accurately estimate capture probabilities. Computational time comparisons reveal the superior efficiency of the new methodologies, with a preference for the analytical approach due to its advantage of best efficiency with similar accuracy to that of the semi-analytical method. The advantage of the analytical methodology is further demonstrated

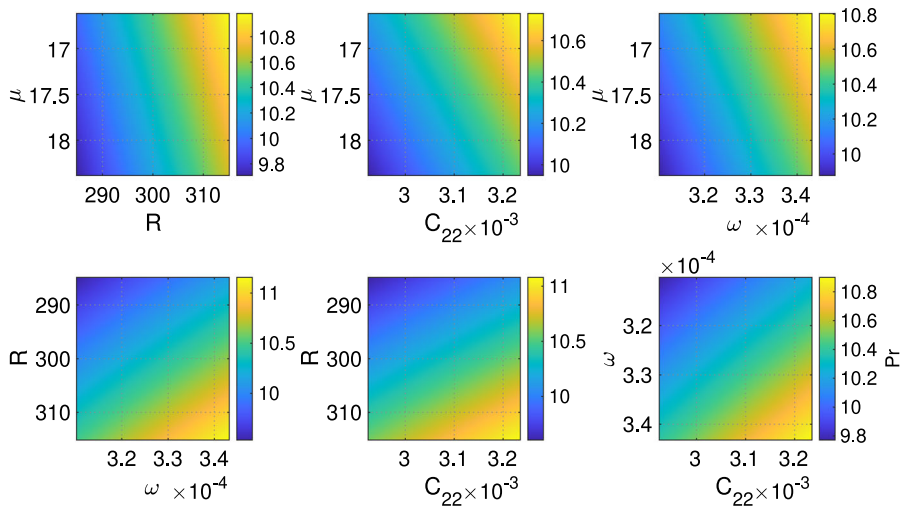

Fig. 11 Probability of capture into 1:1 GTR for a range of μ, R, C_{22} and ω with $e = 0.1$

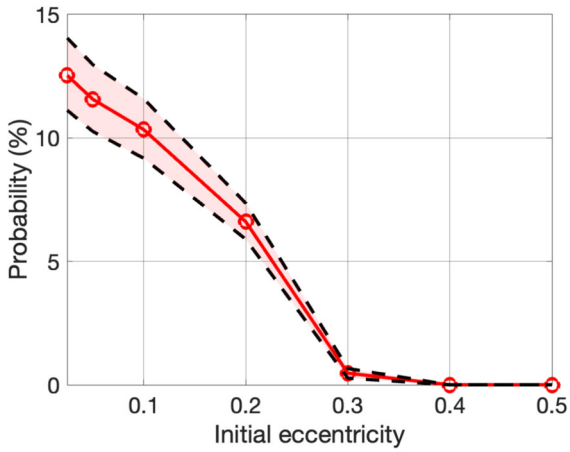

Fig. 12 Probability of capture into 1:1 GTR for different eccentricities values, assuming an uncertainty of 5% on different parameters (in red). The black dashed line represents the absolute uncertainty of the probability

by highlighting potential analysis that can be done to make space exploration missions more robust against the phenomenon of GTR. For future work, it is recommended to further refine these methodologies for scenarios involving high thrust and different inclination values. This would allow the comparison of the estimations obtained with these methodologies with results obtained in previous works [3,21]. Additionally, extending these methodologies to other GTRs, such as the 2:3 GTR around Vesta, could be a valuable area of exploration.

Funding This work is funded by ESA OSIP with the project title "Resonance Capture of Low-Thrust Spacecraft Around a Small Body" and by the John Anderson Research Award Studentship of the University of Strathclyde. Data supporting this study are included within the article and/or supporting materials.

Data Availability Enquiries about data availability should be directed to the authors.

Declarations

Conflict of interest The authors declare that they have no conflict of interest.

References

1. Artemyev, A., Neishtadt, A., Vainchtein, D., Vasiliev, A., Vasko, I., Zelenyi, L.: Trapping (capture) into resonance and scattering on resonance: summary of results for space

plasma systems. Commun. Nonlinear Sci. Numer. Simul. **65**, 111–160 (2018)
2. Garfinkel, B.: On resonance in celestial mechanics. Celest. Mech. Dyn. Astron. **28**, 275–290 (1982)
3. Tricarico, P., Sykes, M.: The dynamical environment of Dawn at Vesta. Planet. Space Sci. **58**, 1516–1525 (2010)
4. Murray, C.D., Dermott, S.F.: Solar system dynamics. Cambridge University Press, Cambridge (2000)
5. Celletti, A., Gales, C., Lhotka, C.: Resonances in the Earth's space environment. Commun. Nonlinear Sci. Numer. Simul. **84**, 105–185 (2020)
6. Lemaitre, A., Delsate, N., Valk, S.: A web of secondary resonances for large A/m geostationary debris. Celest. Mech. Dyn. Astron. **104**, 383–402 (2009)
7. Goldreich, P., Peale, S.: Spin-orbit coupling in the solar system. Astron. J. **71**, 425–438 (1966)
8. Celletti, A., Gales, C.: On the dynamics of space debris: 1:1 and 2:1 resonances. J. Nonlinear Sci. **24**, 1231–1262 (2014)
9. Scheeres, D.J.: Dynamics about uniformly rotating triaxial ellipsoids: applications to asteroids. Icarus **110**, 225–238 (1994)
10. Scheeres, D.J., Ostro, S., Hudson, R., DeJong, E., Suzuki, S.: Dynamics of orbits close to asteroid 4179 Toutatis. Icarus **132**, 53–79 (1998)
11. Scheeres, D.J., Guman, M.D., Villac, B.F.: Stability analysis of planetary satellite orbiters: application to the Europa orbiter. J. Guidance, Control, Dyn. **24**, 778–787 (2001)
12. Paskowitz, M.E., Scheeres, D.J.: Design of science orbits about planetary satellites: application to Europa. J. Guidance, Control, Dyn. **29**, 1147–1158 (2006)
13. Russell, R.: Global search for planar and three-dimensional periodic orbits near Europa. J. Astronaut. Sci. **54**, 199–226 (2006)
14. Lara, M., Russell, R.: Mission design through averaging of perturbed keplerian systems: the paradigm of an Enceladus orbiter. Celest. Mech. Dyn. Astron. **108**, 1–22 (2010)
15. Russell, R., Lara, M.: On the design of an Enceladus science orbit. Acta Astronaut. **65**, 27–39 (2009)
16. Russell, C., Capaccioni, F., Coradini, A., De Sanctis, M.C., Feldmann, W., Jaumann, R., Keller, H., Mccord, T., Mcfadden, L., Mottola, S., Pieters, C., Prettyman, T., Raymond, C., Sykes, M., Smith, D., Zuber, M.: Dawn mission to Vesta and Ceres. Earth Moon Planet. **101**, 65–91 (2007)
17. Rayman, M.D.: Lessons from the Dawn mission to Ceres and Vesta. Acta Astronaut. **176**, 233–237 (2020)
18. Wallace, N., Sutherland, O., Bolter, J., Gray, H., Altay, A., Striedter, F., Budnik, F., Manganelli, S., Montagnon, E., Steiger, C., BepiColombo - solar electric propulsion system operations for the transit to Mercury, 36th International Electric Propulsion Conference, Vienna, (2019)
19. Nishiyama, K., Hosoda, S., Ueno, K., Tsukizaki, R., Kuninaka, H.: Development and testing of the Hayabusa 2 ion engine system. Jpn. Soc. Aeronautical Space Sci. **14**, 131–140 (2016)
20. Morante, D., Sanjurjo Rivo, M., Soler, M.: A survey on low-thrust trajectory optimization approaches. Aerospace **8**, 88 (2021)
21. Delsate, N.: Analytical and numerical study of the ground-track resonances of Dawn orbiting Vesta. Celestial Mech. Dyn. Astronom **59**, 1372–1383 (2011)
22. Scheeres, D.J.: Orbital mechanics about small bodies. Acta Astronautic **72**, 1–14 (2012)
23. Boumchita, W., Feng, J.: The capture probability of Dawn into ground-track resonances with Vesta. Celestial Mech. Dyn. Astron. **136**, 3 (2024)
24. Feng, J., Noomen, R., Hou, X., Visser, P., Yuan, J.: 1:1 ground-track resonance in a uniformly rotating 4th degree and order gravitational field. Celest. Mech. Dyn. Astron. **127**, 67–93 (2017)
25. Lemaître, A., Resonances: Models and Captures. In: Souchay, J., Dvorak, R. (eds) Dynamics of Small Solar System Bodies and Exoplanets, Lecture Notes in Physics, Springer, Berlin, Heidelberg, 790 (2010)
26. Montenbruck, O., Gill, E., Lutze, F.H.: Satellite orbits: models, methods, and applications. Appl. Mech. Rev. **55**, 27–28 (2002)
27. Kaula, W., Theory of satellite geodesy: applications of satellites to geodesy, Blaisdell Publishing Co., (1966)
28. Scheeres, D.J.: The effect of C_{22} on orbit energy and angular momentum. Celest. Mech. Dyn. Astron. **73**, 339–348 (1999)
29. Henrard, J., The Adiabatic Invariant: Its Use in Celestial Mechanics. In: Szebehely, V. (eds) Applications of Modern Dynamics to Celestial Mechanics and Astrodynamics, NATO Advanced Study Institutes Series, 82 (1982)
30. Breiter, S.: Fundamental models of resonance, Monografias de la Real Academia de Ciencias de. Zaragoza **22**, 83–92 (2003)
31. Lhotka, C., Celletti, A., Gales, C.: Poynting-Robertson drag and solar wind in the space debris problem. Mon. Not. R. Astron. Soc. **460**, 802–815 (2016)
32. Okhotsimskii, D., Sikharulidze, Y., Fundamentals of space flight mechanics, (1990)
33. Neishtadt, A.I.: Passage through a separatrix in a resonance problem with a slowly-varying parameter. J. Appl. Math. Mech. **4**, 621 (1975)
34. Neishtadt, A.I.: Averaging method for systems with separatrix crossing. Nonlinearity **30**, 2871 (2017)
35. Shampine, L.F.: Vectorized adaptive quadrature in Matlab. J. Comput. Appl. Math. **211**, 131–140 (2008)
36. Shampine, L.F., Gordon, M.K.: Computer solution of ordinary differential equations: the initial value problem. W. H. Freeman, San Francisco (1975)